2015

A comparison of satellite-derived sea surface temperature fronts using two edge detection algorithms

Yi Chang

Peter C. Cornillon
University of Rhode Island, pcornillon@uri.edu

Citation/Publisher Attribution
Chang, Y., & Cornillon, P. (2015). A comparison of satellite-derived sea surface temperature fronts using two edge detection algorithms. *Deep Sea Research Part II: Topical Studies in Oceanography, 119*, 40-47. doi: 10.1016/j.dsr2.2013.12.001
Available at: https://doi.org/10.1016/j.dsr2.2013.12.001

A comparison of satellite-derived sea surface temperature fronts using two edge detection algorithms

Yi Chang[1], Peter Cornillon[2]

1. Institute of Ocean Technology and Marine Affaris, National Cheng Kung University, 1 University Road, Tainan, Taiwan.
2. Graduate School of Oceanography, University of Rhode Island, Narragansett, RI 02882, USA.

Corresponding author: Yi Chang

E-mail: yichang@mail.ncku.edu.tw

Tel: +886-6-2575575 ext. 31148

Fax: +886-6-2753364

3rd revision and submitted to Deep Sea Research 2, December ?, 2013.

Abstract

Satellite-derived sea surface temperature (SST) fronts provide a valuable resource for the study of oceanic fronts. Two edge detection algorithms designed specifically to detect fronts in satellite-derived SST fields are compared: the histogram-based algorithm of Cayula and Cornillon (1992, 1995) and the entropy-based algorithm of Shimada et al. (2005). The algorithms were applied to four months (July and August for both 1995 and 1996) of SST fields and the results are compared with SST data taken by the *M.V. Oleander*, a container ship that makes weekly transits between New York and Bermuda. There is no significant difference in front pixels found with the Cayula-Cornillon algorithm and those found in the in situ (Oleander) data. Furthermore, for strong fronts, with gradients greater than 0.2 K/km, the distribution of fronts found with the Shimada et al. algorithm is quite similar to that of fronts found with the Cayula-Cornillon algorithm. However, there are significant differences in the number of weak fronts found. This is seen clearly in waters south of the Gulf Stream where the gradient magnitude of fronts found is less than 0.1 K/km. In this region, the probability that the Shimada et al. algorithm detects a front rarely falls below 4% while the other two algorithms find fronts less than 1% of the time. These results raise the question of exactly what qualifies as an SST front, a classic problem in edge detection.

Keywords: edge detection, sea surface temperature front, satellite.

1 Introduction

Oceanic fronts can be defined as relatively narrow zones in which the gradient of a given property is large compared to its background gradient in the region. Although not explicitly defined as gradients in the horizontal, or near horizontal, these are generally the gradients that one thinks of in the context of fronts. Fronts often correspond to boundaries between different water masses or to large shears in currents although other processes may give rise to fronts as well; e.g., a boundary between different vertical mixing regimes on the continental shelf. Of interest in this paper are enhanced horizontal gradients of temperature, specifically, sea surface temperature (SST) fronts.

With the broad availability of satellite-derived SST fields, there has been significant effort devoted to the development of front-detection algorithms – automated methods for detecting fronts in these fields – and to the use of the resulting front data sets in scientific investigations. Front-detection algorithms fall into several categories, three of which are relevant here: gradient algorithms (Moore et al., 1997), histogram algorithms (Cayula and Cornillon, 1992, 1995; CCA, referring to the Cayula-Cornillon Algorithm, hereafter), and entropy algorithms (Vazquez et al., 1999; Shimada et al., 2005; SEA, referring to the Shimada Entropy Algorithm, hereafter). These algorithms have been applied to thermal fronts in marginal seas (Hickox et al., 2000; Wang et al., 2001; Belkin and Cornillon, 2003) as well as open ocean regions (Ullman et al., 2007; Belkin et al., 2009). Several studies have also presented new views of oceanic fronts in coastal and regional seas, such as Ullman and Cornillon (1999) who applied the CCA to the northeastern coast of the US, and Shimada et al. (2005) and Chang et al. (2006, 2010) who applied SEA to the Japanese coast and northern South China Sea. Interestingly, the West Luzon Front detected by CCA in Belkin and Cornillon (2003) and by SEA in Chang et al. (2010) was not detected by Wang et al. (2001) in their application of a gradient based algorithm to SST fields of the northern South China Sea. This suggests that the gradient based approach may not be appropriate for the detection of SST fronts in regions of weak SST gradients (Chang et al., 2010).

When applying automated algorithms of front detection to satellite images, it is important to verify these methods. Ullman and Cornillon (2000) used SST fronts detected in along-track ship data to evaluate CCA detected fronts in satellite-derived fields. Fronts were identified in the in situ data based on along-track SST gradients. In this paper, we compare CCA and SEA detected fronts in satellite-derived SST fields with one-another and with fronts detected from continuous temperature measurements conducted from a merchant ship in transit between New York and Bermuda, the same basic data set used by Ullman and Cornillon (2000). We do not include comparison with a gradient based algorithm applied to the satellite-derived SST fields because this was dealt with in detail in Ullman and Cornillon (2000). The result of that analysis was that the gradient based algorithm found false fronts at roughly twice the rate that CCA did.

2 Data and methods

Full resolution (1.2 km) July and August SST fields from both 1995 and 1996 were used for this study. These fields were derived from the level 2b (L2b)[1] Advanced Very High Resolution Radiometer (AVHRR) data in the University of Miami/University of Rhode Island (URI) archive with version 5.0 of the National Oceanic and Atmospheric Administration (NOAA)/National Aeronautics and Space Administration (NASA) Pathfinder algorithm (Smith et al. 1996). Data in the archive cover the waters off the northeastern coast of the United States and the southeastern coast of Canada, east to approximately 40°W. Following retrieval to L2b, the 2 to 4 passes available per day were manually navigated to within 1 pixel, ~1.1 km at nadir. The fields were then remapped to an equirectangular projection (L3) with 1.2 km pixel spacing at the image center, 38°N 70°W. Remapping from L2b was performed using the nearest neighbor L2b pixel to the target L3 pixel. The study area used for this project (Fig. 1), 78° to 63°W and 31°to 43°N, was extracted from these fields. Cloud removal was performed using the URI multi-image cloud detection algorithm described in Ullman and

[1] We use the NASA designation for data processing levels: http://science.nasa.gov/earthscience/earth-science-data/data-processing-levels-for-eosdis-data-products/.

Cornillon (1999). Detection of fronts in declouded SST images was performed using both the CCA and SEA methods. Brief descriptions of these are given below. More detailed descriptions are available in the original references (Cayula and Cornillon, 1992, 1995 for CCA; Vazquez et al., 1999 and Shimada et al., 2005 for SEA).

2.1 Front Detection Using Satellite-Derived Data

The Cayula-Cornillon algorithm (CCA) used in this study is the multi-image version of the original multi-image edge detection algorithm developed at URI. In the first step, the SST fields are median filtered with a 3x3 (3.6x3.6 km) kernel to reduce noise in the field. This provides for a sharper separation of peaks corresponding to different water masses in the histograms used in the next step. Reducing the noise in the image is also beneficial in the contour following step. In the second step, the single image edge detector (SIED) is applied to each image in the time series. The SIED performs a set of statistical tests on histograms of the temperature field in a moving *n*x*n* (32x32 in this study) pixel window to identify candidate front pixels. It then descends to the pixel level and follows contours identified by the candidate front pixels. Segments shorter than *m* (10 in this study) pixels are subsequently eliminated from consideration. A second pass is then made over the images in the archive. First a zero-one image, initialized to zero, is formed in which each pixel flagged as a front pixel in any image within *n* (60 in this study) hours of the given image, excluding the image of interest, is set to one. (It is important to note that the window used here does not exclude shorter time scale fronts; any front found in any of the adjacent images is included. Furthermore, this step is used to 'help' the algorithm find fronts in areas partially contaminated by clouds, it does not eliminate fronts.) The resulting image is then thinned, based on the local SST gradient, to lines one pixel wide. In the last step, the SIED algorithm is applied a second time to each image in the archive, but this time it uses the thinned persistent fronts associated with that image in the contour following step along with candidate pixels found in the analysis of histograms in the image. Fig. 2b shows fronts resulting from this procedure for the AVHRR-derived SST field shown in Fig. 2a.

The Shimada et al. algorithm is specifically designed for finer-scale front detection at the full image resolution of 1.2 km (Shimada et al., 2005). As typically employed, the original SST fields are not filtered prior to application of this algorithm. However, for comparison with CCA, SEA has been applied to both the original data, as is normally done, and to the 3x3 median filtered version of the data. Edge detection begins with an estimate of the Jensen-Shannon divergence in SST in two 5x5 pixel subwindows in four directions (shown in Fig. 3 of Shimada et al., 2005). A composite matrix is built from the four Jensen-Shannon divergences, and the maximum value is taken as the final divergence value to be assigned to each pixel. If this value exceeds 0.6 then the pixel is designated a front pixel. Finally, a thinning algorithm is applied to obtain pixel wide frontal segments. The results, again for the SST field in Fig. 2a, are shown in Fig. 2c for the unfiltered SST field and in Fig 2e for the 3x3 median filtered field. However, in order to compare this with CCA derived fronts, frontal segments shorter than 10 pixels are removed from further comparisons. These fronts are shown in Figs. 2d and 2f. Following front-detection, the SST gradient was calculated at each front pixel resulting from each of the two algorithms using the Prewitt operator to obtain the latitudinal and longitudinal gradient components. The gradient magnitude, $|T_s|$ where T_s is SST, was determined from the Prewitt components.

2.2 Processing of Ship Measurements

Comprehensive validation of the Cayula-Cornillon algorithm for satellite-derived SST images using in situ data is described by Ullman and Cornillon (2000). In this study we compare SEA and CCA detected fronts with fronts detected in continuous ocean temperature measurements made from the container vessel *M.V. Oleander* (*Oleander* in the remainder), which regularly navigates between Port Elizabeth, NJ and Bermuda. The mean ship track is superimposed on Fig. 1 (black line). The *Oleander* temperature data were measured by a flow system at a depth of between 5 and 6 m sampled every 15 s, a corresponding spatial sampling of approximately 110 m at a ship speed of 15 knots. For comparison with the AVHRR data, the *Oleander* data were averaged to a 1.2 km spacing along the ship's track. SST fronts in the *Oleander* data were identified by their along-track gradient as described in Ullman and Cornillon (2000). Specifically, an along-track location was defined as a front if one of two criteria was met. (1) The SST gradient magnitude exceeded 0.2 K/km or (2) SST gradient magnitude exceeded 0.1 K/km and the gradient magnitude at the along-track location was five times larger than the mean gradient magnitude averaged over a 70 km section centered on the point of interest – the definition of a front used by Fedorov (1986). For the comparisons undertaken in this study, only satellite-derived SST fronts intersecting a ship track within 6 h of the passage of the ship were selected for further analyses.

3 Results

3.1 SST Front Probability and Mean Gradient Maps

Monthly composite maps of front probability were produced from the fronts detected in the individual satellite-derived images for June to August in both 1995 and 1996. Front probability at a pixel is defined as the number of times the pixel was designated as a front pixel in the period considered divided by the number of times the pixel was clear in the same period. Fig. 3 shows the CCA (Fig. 3a) and the SEA (Fig. 3b, c and d) SST front probabilities for August 1995. The CCA (3a) front probability map shows several frontal bands between Cape Hatteras (white arrow) and Georges Bank (yellow arrow). Most of these bands are approximately parallel to the 100 m isobath with front probabilities as high as 11%. In contrast, front probabilities in the unfiltered SEA[2] map (3b) are everywhere substantially larger, up to 16% at some locations on the continental shelf, than those in the CCA-derived field. SEA front

[2] 'Unfiltered' here refers to the SST fields from which the fronts were derived. It does not refer to filtering, or the lack thereof, of the probability fields. 'Filtered' SEA fields refers to the application of a 3x3 median filter to the SST fields prior to the application of SEA. This convention will be used througout this manuscript.

probabilities obtained after eliminating front segments less than 10 pixels long from the unfiltered data (Fig. 3c), although less than the corresponding probabilities in the full SEA field (expected since a significant number of front pixels have been removed from the data), are still higher than the corresponding CCA probabilities. This is especially evident across much of the southern part of the study area; e.g., the area indicated by the red arrow. In contrast, the front probabilities for the filtered fields with front segments shorter than 10 pixels removed (Fig. 3d) are quite different than the unfiltered version (Fig. 3c). Specifically, the filtered data show a significant decrease in front probability on the shelf when compared to the unfiltered probabilities and a significant increase in waters seaward of the Gulf Stream. In both cases – the increase in front probability seaward of the Gulf Stream and its decrease shoreward – well know structures in this region, such as the Gulf Stream and the Shelf Break front clearly evident in the CCA probability field (Fig. 3a) and to a lesser extent in the unfiltered SEA field (Fig. 3c), tend to be all but eliminated in the filtered field (Fig. 3d). In light of this, the focus of the remainder of this manuscript will be on comparisons of unfiltered SEA probabilities with CCA probabilities and front locations in the in situ data.

Fig. 4a shows the mean SST gradient magnitude, $|\nabla T_s|$, for August 1995 at CCA detected front locations and Figs. 4b and c, the corresponding SEA fields. These mean fields were obtained only from gradient values when a front was present. Specifically, if a front was detected by CCA at location x, y in images A and B, but not in image C, only $|\nabla T_s|$ from images A and B were used when calculating the mean at x, y. In most locations, the CCA front $|\nabla T_s|$ is larger than the corresponding SEA value. This is because SEA finds more fronts, many of which tend to be weaker (as will be shown shortly and discussed in more detail in Section 4) than those found by CCA, thus reducing the mean value. The same behavior is observed when comparing the full SEA detected $|\nabla T_s|$ field (Fig. 4b) with that obtained from the reduced SEA data set (Fig. 4c); i.e., after the removal of short and presumably weaker frontal segments. The CCA front $|\nabla T_s|$ map shows that mean fronts in the study area tend to be stronger, with values approaching 0.3 K/km, along the shelf-break than elsewhere in the region. The largest values occurred on the southeastern flank of Georges Bank. The mean front $|\nabla T_s|$ values along the shelf-break are consistent with those found by Ullman and Cornillon (1999) for the climatological summer, July through September, based on data from 1985 through 1996. Although the SEA front $|\nabla T_s|$ map (Fig. 4b) shows similar patterns on the periphery of Georges Bank, with the strongest values >0.3 K/km, the pattern in much of the remainder of the study area reveals substantial differences between the

CCA and SEA front gradient fields. Frontal bands clearly seen in the CCA composite are only vaguely discernible in the SEA composite; e.g., along the northern and southern boundaries of the Gulf Stream (white arrows in Fig. 4a, b). However, the SEA front $|\nabla T_s|$ map generated with short fronts eliminated (Fig. 4c), is more similar to the CCA map than is the SEA map based on all detected fronts. This suggests that much of the difference in the performance of the two edge detection algorithms is related to short, weak front segments found by the SEA but not by CCA.

3.2 Comparison of AVHRR with Along-Track Fronts

Fig. 5 shows a comparison of *Oleander* SSTs (black line) and Pathfinder SSTs (gray line) for 2-4 June 1995 - cruise MB9506a. To obtain this plot, the 9 AVHRR SST values (a 3x3 pixel square) nearest each *Oleander* sample in space and within 6 hours in time were averaged. Cloud contaminated pixels were not included in the average. Given that AVHRR passes are separated by approximately 12 hours this results in a value at virtually all *Oleander* locations (with temporal and spatial sampling of 15 s and 110 m, respectively), cloud cover permitting. The large scale changes in SST are well represented in both data sets shoreward of ~600 km - both see the very large change in SST at the shelf-break, ~200 km from New York, and the somewhat more gentle increase at approximately 450 km associated with the shoreward edge of the Gulf Stream. However, seaward of ~630 km there is a notable difference in the trends. SST in the *Oleander* record decreases rather abruptly at ~630 km, corresponding to the seaward, or southern, edge of the stream, and then remains relatively constant at about 22°C for the remainder of the transect, In contrast, AVHRR SSTs decrease at a very nearly constant rate from their peak of 26°C in the Gulf Stream (~500 km) to ~20°C toward the end of transect. Given that the Oleander data is warmer than the AVHRR data in this region, it is unlikely that the difference is due to the difference in depth at which the observations are made - 5 to 6 m for the *Oleander* and the top 10μm for AVHRR - since one would expect deeper waters to be slightly cooler than surface waters, not warmer. The more likely explanation is that high, thin clouds or small, unresolved clouds are depressing the satellite-derived SST values seaward of the southern edge of the Gulf Stream. A significant increase in cloud cover south of the stream is evident in the images for 2-4 June (not shown) supporting this view. Although pixels contaminated in this way are not likely to introduce false fronts in the CCA results and most likely not in the SEA results, they are likely to depress SST retrievals.

The locations of fronts found with the three different methods (SEA fronts are only those with at least 10 pixels per front segment) are also indicated in Fig. 5. Consistent with Figs. 2 and 3, significantly more fronts are found by SEA than CCA. Significantly more fronts are also found in the Oleander data than by CCA, but these, as with the fronts located by CCA, tend to cluster in regions of large SST gradients while the SEA fronts tend to be more uniformly distributed. Note that no fronts are found seaward of about 900 km by CCA or in the Oleander data while there is a significant number found by SEA. Fig. 6 is a statistical summary in histogram form of the location of fronts, as defined by the various algorithms, along the Oleander track for all ship sections in June and August of 1995 and 1996. Histogram bins correspond to 20 km along-track sections, ~16 AVHRR pixels. A peak located approximately 200 km from New York is evident for all three algorithms (Figures4a-c). The location of these peaks corresponds to the location of the 200 m isobath and the associated shelf-break front; i.e., to the high gradient region evident at 200 km in Fig. 5. There are also two relatively well-defined peaks at approximately 420 km and 530 km in the *Oleander* histogram. These correspond to the mean positions of the in-shore edge of the Gulf Stream, sometimes referred to as the 'North Wall', and the southern edge of the stream, respectively; the approximate location of the high gradient regions seen in the Oleander data at ~450 km and ~630 km in Fig. 5. The correspondence is not exact because of the lateral displacement of the Gulf Stream. There is a suggestion of peaks in the same locations in the CCA and SEA data. However, there are a number of other peaks in the SEA data that do not correspond to any in the *Oleander* data confounding the interpretation of the Gulf Stream peaks. The clearest difference between the histograms is in the larger number of SEA fronts compared with both CCA and Oleander fronts in all bins. This is discussed in more detail in the next section.

4 Discussion and Conclusion

Comparisons of along-track fronts discussed in the previous section reveal clear differences between the satellite and the in situ data. Table 1 shows the results of an analysis of Variance (ANOVA) information table testing the number of front pixels per 20 km bin detected by the in-situ, CCA, and SEA algorithms. There is a significant difference between the numbers of fronts in the three datasets ($p<0.05$). We therefore compared the difference in numbers between pairs of datasets. For the *Oleander*-CCA pair, there are no obvious differences; the null hypothesis cannot be rejected. However, the numbers of front pixels are significantly different between the *Oleander* and SEA and between the CCA and SEA, datasets.

The ANOVA tests establish the statistical significance of the difference in the mean number of fronts per bin between SEA and CCA, and SEA and in situ, but not in the shapes of the distributions. In fact, the increased number of detected fronts in the SEA data appears to be fairly uniformly distributed along the *Oleander* track. Specifically, the SEA histogram (Fig. 6c) decreases from a maximum at 200 km, the shelf-break front, to approximately 600 km, seaward of which it is close to flat at about 90 detected front pixels per 20 km bin, while seaward of 600 km CCA and Oleander histogram values (Figs. 6a & b) are, on average, less than 10 detected fronts per bin. The 80 front difference is slightly smaller than, but close to, the difference, approximately 100 fronts, between the height of the shelf-break peak at 200 km in the SEA histogram (220 fronts) and that in the Oleander histogram (120 fronts). This suggests a background level of front detection for the entropy algorithm of about 8%; there are on average 80 cloud free pixels for the four month study period at each (1.2 km) location along the *Oleander* track seaward of 600 km and there are 16 AVHRR pixels (and along-track *Oleander* samples) in each 20 km bin yielding a total of approximately 1300 clear pixels in each bin. This results in a probability on the order of 90/1300 (approximately 7%) close to the values evident in Fig. 3c for this portion of the track. In fact, the general differences in the SEA probability distribution (Fig. 3c) from the CCA distribution (Fig. 3a) are consistent with the argument presented above for a relatively flat background detection rate along the *Oleander* track.

In the previous paragraphs we have shown that there is a relatively uniform background of SEA detected fronts to which are added fronts associated with major features from the shelf to the outer edge of the Gulf Stream. In Section 3 we also suggested that the fronts seen seaward of the Gulf Stream tend to be weak and likely short. Here we revisit these observations. Ullman and Cornillon (2000) suggest that the error rate in CCA front detection is >40% when the temperature gradient is <0.1 K/km but falls rapidly with increasing SST gradient magnitude. Comparing the CCA gradient map (Fig. 4a) with the SEA map based on eliminating short fronts (Fig. 4c), it is clear that strong SST fronts, >0.2 K/km, those along the shelf-break especially in the vicinity of Georges Bank are well represented in both fields. This is similar to the results of Ullman and Cornillon (2000) that front pixels with high $|\nabla T_s|$ are well defined. However, pixels with gradients about 0.1 K/km are clearly seen in offshore waters in the SEA composite maps (Fig. 4b, c) but are not found in the CCA results (Fig. 4a). We further investigated the spatial distribution of front pixels detected by CCA and SEA in the single image shown in Fig. 7. CCA and SEA detected frontal segments (Fig. 7a and b) correspond well in the Gulf Stream and along the shelf-break around Georges Bank. However, SEA found many more frontal segments in the study area (Fig. 7b, with fronts of < 10 pixels omitted) than the CCA algorithm. When frontal segments from both algorithms are superimposed (Fig. 7c), it is clearly seen that CCA frontal segments (blue lines) are mainly distributed in coastal waters. In contrast, the SEA segments (red lines) are evident throughout the image with a slightly higher density on the shelf than in Slope, Gulf Stream or Sargasso Sea waters. This is consistent with the number of fronts found along the track of the *Oleander* discussed in Section 3. Also note that the SEA frontal segments tend to be substantially shorter on average than the

CCA segments.

Following Ullman and Cornillon (2000), we also examine the error rate in detection of SST fronts by CCA and SEA compared with the in situ data. False front errors occur if the ship was at the location of an AVHRR front within 6 hours of the AVHRR image time and a front was not found in the ship data. The error rates for each of the two satellite-based algorithms are shown in Fig. 8 as a function of the SST gradient associated with the front. The results for CCA compare well with those of Ullman and Cornillon (2000). They are also consistently lower than the corresponding error rate for SEA with the fractional discrepancy increasing substantially with SST gradient.

So why might the entropy algorithm (SEA) find more fronts than the histogram algorithm (CCA) or the gradient algorithm applied to the in situ data? Initially, one might think that the main reason for the discrepancy relates to the preprocessing of the SST fields, specifically, to the median filtering of the fields. However, a comparison of front probabilities obtained from SEA applied to the filtered SST fields with those obtained from SEA applied to the unfiltered fields and to those obtained from CCA suggest that this is not the case. Specifically, CCA tends to find fronts preferentially on the continental shelf relative to waters seaward of the Shelf Break while SEA applied to the filtered SST fields finds just the opposite, it finds fronts preferentially in waters seaward of the Shelf Break. Furthermore, SEA applied to the unfiltered data, the results discussed in some detail in previous sections, tends to find fronts preferentially on the shelf as did CCA although at a much higher density. Other factors that might contribute to the entropy algorithm finding more fronts than the CCA and in situ algorithms are:

(1) The size of the region examined by the algorithms (SEA vs. CCA): CCA identifies two populations in 32x32 pixel histograms and uses the boundary pixels between these populations to begin contour following. This means that if there are more than two distinct populations in the window, the algorithm will miss fronts. The fronts found will tend to be those between the largest two populations. The entropy algorithm operates on 5x5 pixel subwindows, hence it is not constrained to the same extent. The gradient algorithm applied to the in situ data used an even smaller kernel.

(2) The effect of clouds on the retrieval of fronts (SEA vs. CCA, and SEA and CCA vs. in Situ): As noted earlier, the histogram of SST fronts for the Oleander data (Fig. 6a) shows two peaks associated with the Gulf Stream, one corresponding to the northern edge at ~400 km and one to the southern edge at ~520 km and then it drops precipitously from between 50 and 60 counts to ~20 counts after which it is relatively flat. Over the same region the CCA and SEA histograms decrease

relatively smoothly from their values at 280 km to their values at 500 km after which they too are relatively flat. There is a corresponding decrease in the percent of pixels identified as 'clear' by the Pathfinder algorithm (not shown) from 280 to 500 km. This increase in cloud cover is likely the cause of the differences in numbers of fronts found by the different algorithms. Because the CCA operates on 32x32 pixel histograms and requires at least 100 clear pixels to perform the histogram analysis and because it requires fronts to be at least 10 pixels long, its performance decreases as cloud cover increases; i.e., the algorithm will miss fronts in small clear regions. The SEA, which operates on smaller regions, is less susceptible to this problem hence will find relatively more fronts than the CCA as the cloud cover increases. The in situ algorithm does not depend on cloud cover at all although a match-up is not attempted if the satellite-data are not clear in the vicinity of the pixel of interest.

(3) The dimensionality of the data (SEA and CCA vs. in situ): Both CCA and SEA operate on two-dimensional fields while the in situ algorithm operates on a line. The two dimensionality of satellite-derived SST fields allows for a weaker gradient or temperature threshold (depending on the algorithm) than that for the gradient algorithm applied to the one dimensional data; i.e., the 2d algorithms incorporate

information from the second dimension in the detection of fronts.

In conclusion, the entropy algorithm finds many more weaker and likely shorter, fronts than the histogram or the in situ gradient algorithms. Although many of these fronts are likely real, the large number of weak fronts tends to mask the stronger fronts in statistical analyses of front distribution. This problem might be addressed by applying a filter to the SEA fronts; e.g., filtering on length, as we did here, and/or on $|\nabla T_s|$. The difficulty with applying filters, especially on the gradient, is what to use as a threshold. This is one of the advantages of the histogram algorithm; it is relatively insensitive to the gradient. In the end, the appropriate algorithm to use will depend on the application, specifically, on what is considered to be a front for the application. The histogram algorithm was designed to find long fronts separating two relatively large water masses, fronts that are thought to be dynamically important; i.e., to extend deeper in the water column than short, weak fronts. The latter may, however, be of significance in biological or chemical studies and of indicators of some submesoscale ocean structures.

Acknowledgements

This study was supported by a research grant (NSC96-2917-I-019-102) from the

National Science Council, Taiwan. Salary support for P. Cornillon was provided by the state of Rhode Island and Providence Plantations. The authors wish to thank Prof. Hiroshi Kawamura, Dr. Futoki Sakaida, and Dr. Teruhisa Shimada of Tohoku University, Japan for their technical support and advice and Dr. Igor Belkin of the University of Rhode Island, USA for helpful advice on this manuscript.

Figure captions:

Table 1: ANOVA table for the number of fronts detected by the Oleander, CCA and SEA methods.

Figure 1: Topographic features of the study area off the northeast United States redrawn from Ullman and Cornillon (1999). CH, NY, LI, and GB indicate the Cape Hatteras, New York, Long Island, and Georges Bank, respectively.

Figure 2: (a) AVHRR- SST for 0640 GMT 1 August 1995; (b) frontal segments obtained from CCA applied to the 3x3 median filtered SST field of panel a; (c) frontal segments obtained from SEA applied to the unfiltered SST field of panel a; (d) frontal segments following removal of all segments shorter than 10 pixels obtained from SEA applied to the unfiltered SST field of panel a; (e) frontal segments obtained from SEA applied to the 3x3 median filtered SST field of panel a, and; (f) frontal segments following removal of all segments shorter than 10 pixels obtained from SEA applied to the 3x3 median filtered SST field of panel a.

Figure 3: Monthly maps of SST front probability detected by (a) CCA applied to the 3x3 median filtered SST fields; (b) SEA applied to the unfiltered SST fields; (c) SEA applied to the unfiltered SST fields, with frontal segments shorter than 10 pixels removed, and; (d) SEA applied to the 3x3 median filtered SST fields, with frontal segments shorter than 10 pixels removed.

Figure 4: Monthly composite maps of SST gradient magnitude detected by (a) CCA applied to the 3x3 median filtered SST fields; (b) SEA applied to the unfiltered SST fields and; (c) SEA applied to the unfiltered SST fields, with frontal segments shorter than 10 pixels removed.

Figure 5: Along-track SST for 2 to 4 June 1995 obtained from the Oleander (black line) and AVHRR (gray line).

Figure 6: Histogram distribution in 20 km bins of front pixels detected along the Oleander track from (a) in-situ SST; (b) CCA applied to the 3x3 median filtered SST fields and; (c) SEA applied to the unfiltered SST fields, with frontal segments shorter than 10 pixels removed.

Figure 7: (a) SST for 1806 GMT 1 August 1995 with CCA detected fronts superimposed; (b) The same image with SEA detected fronts, obtained from the unfiltered field, superimposed and; (c) CCA detected fronts (blue) and SEA detected fronts (red) from the same SST field.

Figure 8: Error rate in detection of SST fronts by CCA and SEA (unfiltered) compared with the in situ data as a function of the gradient along the Oleander track.

References

Belkin, I., Cornillon, P.C., 2003. SST fronts of the Pacific coastal and marginal seas. Pacific Oceanography, 1 (2), 90–113.

Belkin, I.M., Cornillon, P.C., Sherman, K., 2009. Fronts in Large Marine Ecosystems. Prog. Oceanogr. 81 (1-4), 223-236, doi:10.1016/j.pocean.2009.04.015.

Cayula, J.F., Cornillon, P., 1992. Edge detection algorithm for SST images. J. Atmos. Ocean. Technol. 9 (1), 67-80.

Cayula, J.F., Cornillon, P., 1995. Multi-image edge detection for SST images. J. Atmos. Ocean. Technol. 12 (4), 821-829.

Chang, Y., Shimada, T., Lee, M.A., Lu, H.J., Sakaida, F., Kawamura, K., 2006. Wintertime sea surface temperature fronts in the Taiwan Strait. Geophys. Res. Lett. 33 (23), L23603, doi:10.1029/2006GL027415.

Chang, Y., Shieh, W.J., Lee, M.A., Chan, J.W., Lan, K.W., Weng, J.S., 2010. Fine-scale sea surface temperature fronts in wintertime in the northern South China Sea. Int. J. Remote Sens. 31 (17-18), 4807-4818.

Fedorov, K.N., 1986. The physical nature and dtructure of oceanic fronts. Lect. Notes Coastal Estuarine Stud., 19, 333 pp., AGU, Washington, D. C., doi:10.1029/LN019.

Hickox, R., Belkin, I., Cornillon, P., Shan, Z., 2000. Climatology and seasonal variability of ocean fronts in the East China, Yellow and Bohai seas from satellite SST data. Geophys. Res. Lett. 27 (18), 2945-2948.

Moore, J.K., Abbott, M.R., Richman, J.G., 1997. Variability in the location of the Antarctic Polar Front (90°-20°W) from satellite sea surface temperature data. J. Geophys. Res. 102 (C13), 27825-27833.

Shimada, T., Sakaida, F., Kawamura, K., Okumura, T., 2005. Application of an edge detection method to satellite images for distinguishing sea surface temperature fronts near the Japanese coast. Remote Sens. Environ. 98 (1), 21-34.

Ullman, D.S., Cornillon, P.C., 1999. Satellite-derived sea surface temperature fronts on the continental shelf off the northeast U.S. coast. J. Geophys. Res. 104 (C10), 23459-23478.

Ullman, D.S., Cornillon, P.C., 2000. Evaluation of front detection methods for satellite-derived SST data using in situ observations. J. Atmos. Ocean. Technol. 17 (12), 171667-1675.

Ullman, D.S., Cornillon, P.C., Shan, Z., 2007. On the characteristics of subtropical fronts in the North Atlantic. J. Geophys. Res. 112 (C1), C01010, doi:10.1029/2006JC003601.

Vazquez, D.P., Atae-Allah, C., Luque-Escamilla, P.L., 1999. Entropic approach to edge detection for SST images. J. Atmos. Ocean. Technol. 16 (7), 970-979.

Wang, D., Liu, Y., Qi, Y., Shi, P., 2001. Seasonal variability of thermal fronts in the Northern South China Sea from satellite data. Geophys. Res. Lett. 28(20), 3963-3966.

Table 1:

ANOVA Table of Detected Fronts						
Number of Fronts/Methods		Sum of Square	df	Mean Square	*F*	P
In-situ, CCA and SEA *	Between	252839.28	2	126419.64	76.51	3.79E-22
	Within	198274.88	120	1652.29		
In-situ and CCA	Between	679.22	1	679.22	0.64	0.43
	Within	84952.83	80	1061.91		
In-situ and SEA *	Between	200623.61	1	200623.61	111.43	8.06E-17
	Within	144041.27	80	1800.52		
CCA and SEA *	Between	177956.1	1	177956.1	84.97	3.28E-14
	Within	167555.66	80	2094.45		

(*: Indicates there is a significant difference between methods.)

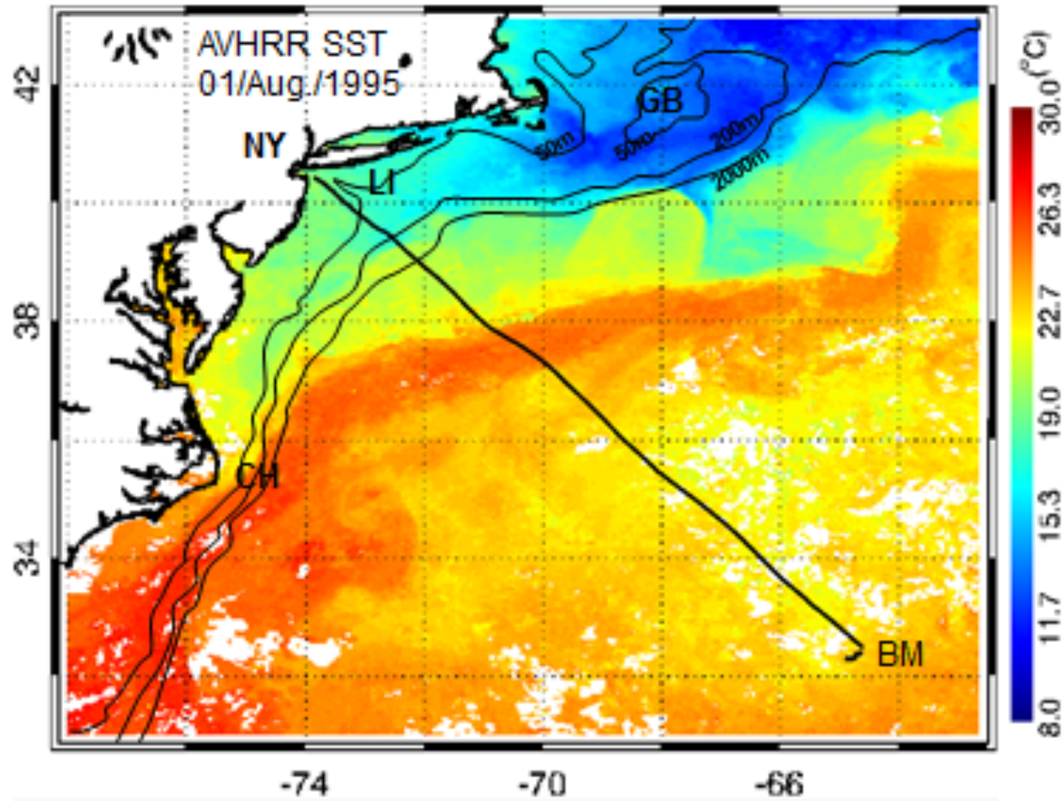
AVHRR SST
01/Aug./1995
NY
LI
GB
CH
BM
50m
200m
2000m
42
38
34
-74
-70
-66
(°C)
30.0
26.3
22.7
19.0
15.3
11.7
8.0

Figure 1.

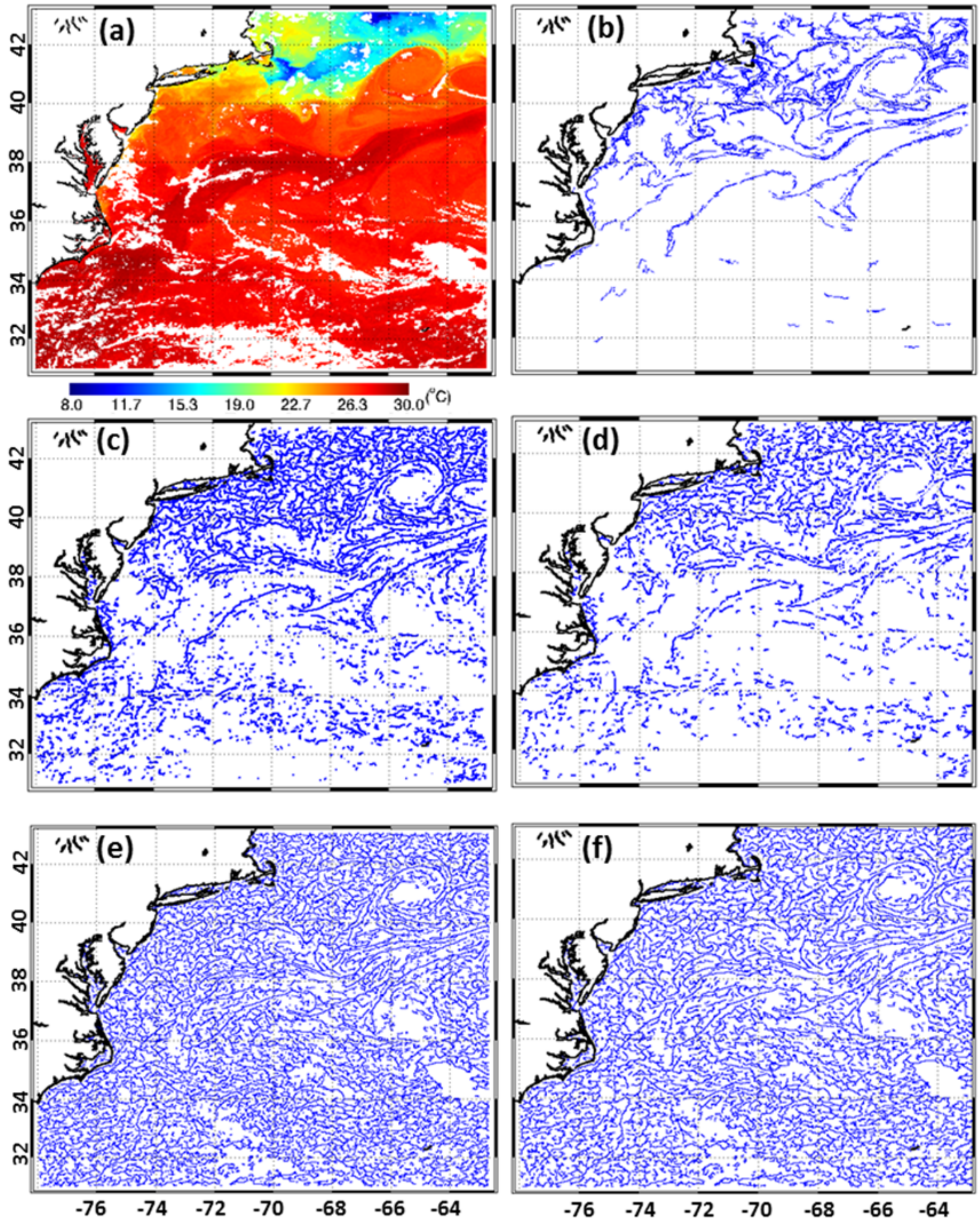
(a)
(b)
(c)
(d)
(e)
(f)
8.0
11.7
15.3
19.0
22.7
26.3
30.0
(°C)
42
40
38
36
34
32
-76
-74
-72
-70
-68
-66
-64

Figure 2.

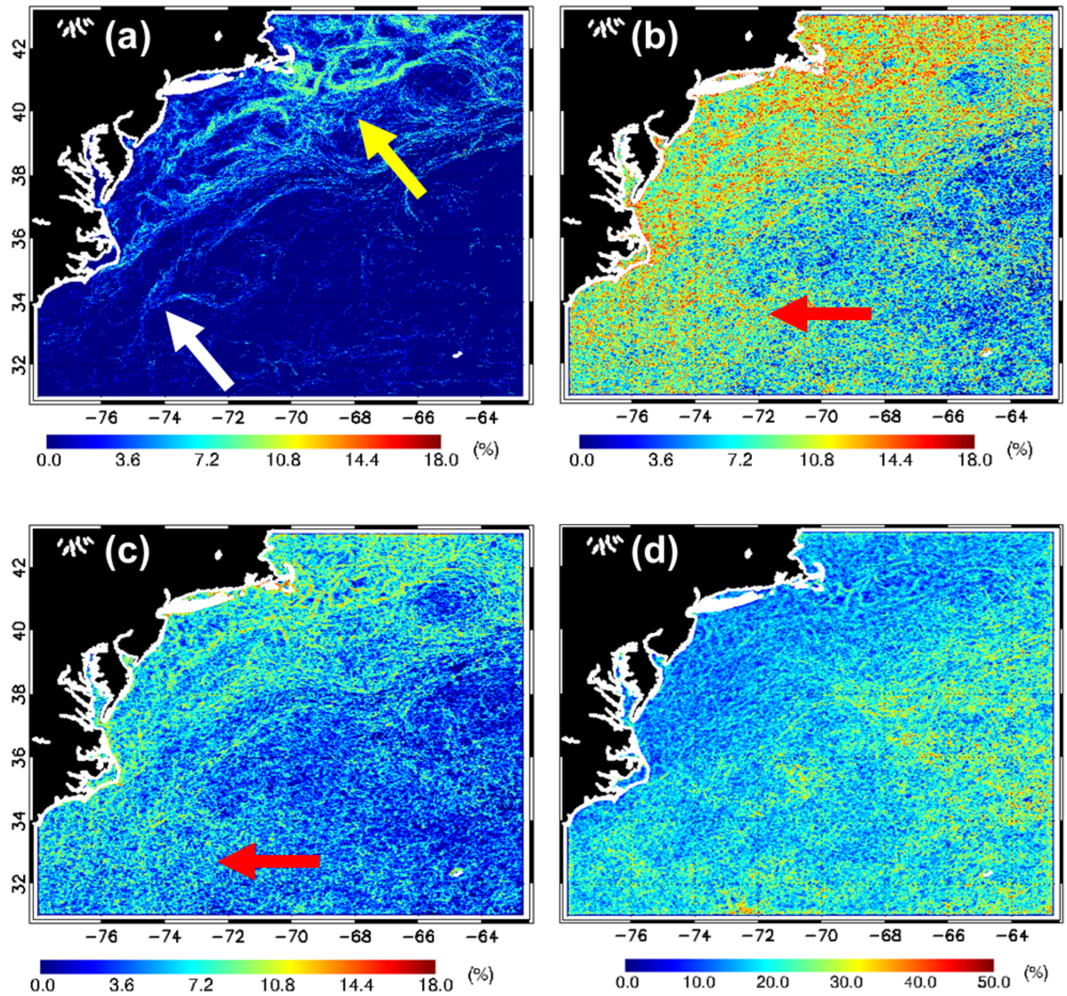

(a)
(b)
(c)
(d)
42
40
38
36
34
32
−76
−74
−72
−70
−68
−66
−64
0.0
3.6
7.2
10.8
14.4
18.0
(%)
10.0
20.0
30.0
40.0
50.0

Figure 3.

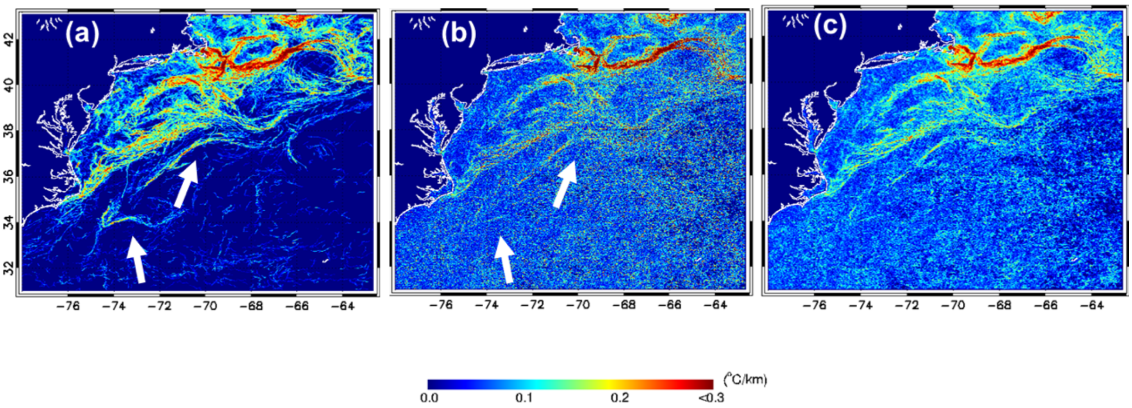

Figure 4.

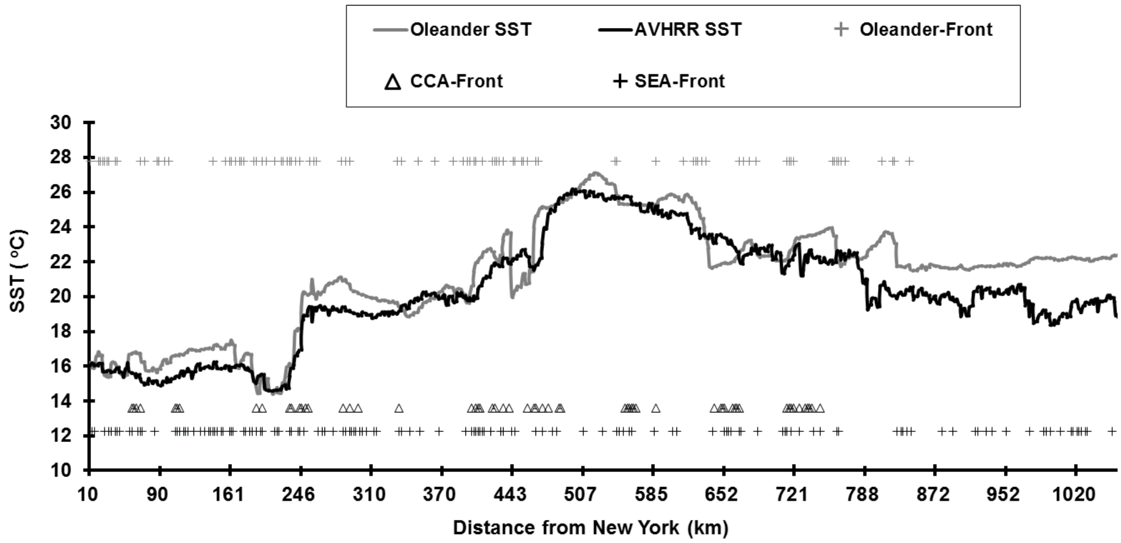
Oleander SST
AVHRR SST
Oleander-Front
CCA-Front
SEA-Front
SST (°C)
Distance from New York (km)
30
28
26
24
22
20
18
16
14
12
10
10
90
161
246
310
370
443
507
585
652
721
788
872
952
1020

Figure 5.

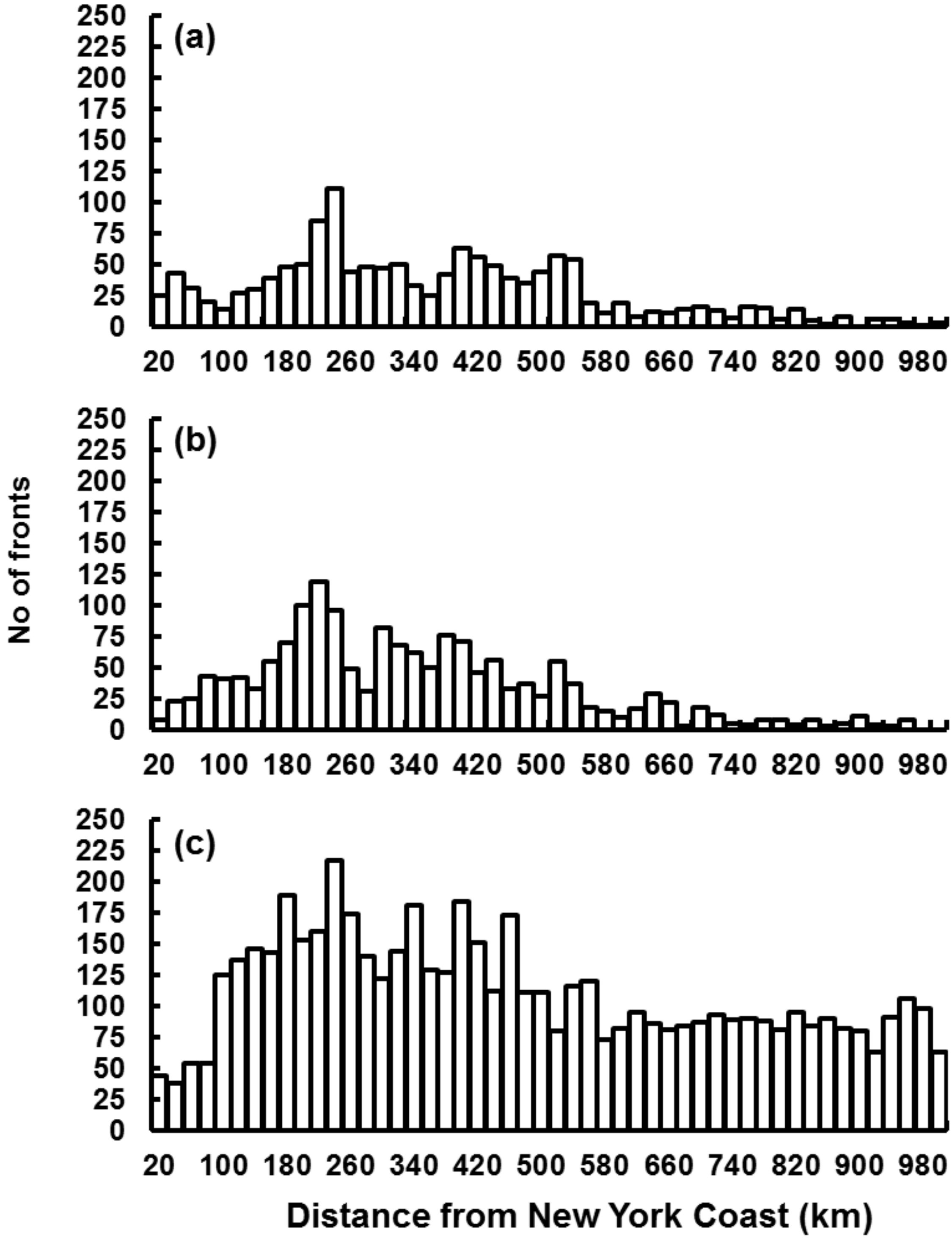
(a)
(b)
(c)
0 25 50 75 100 125 150 175 200 225 250
20 100 180 260 340 420 500 580 660 740 820 900 980
No of fronts
Distance from New York Coast (km)

Figure 6.

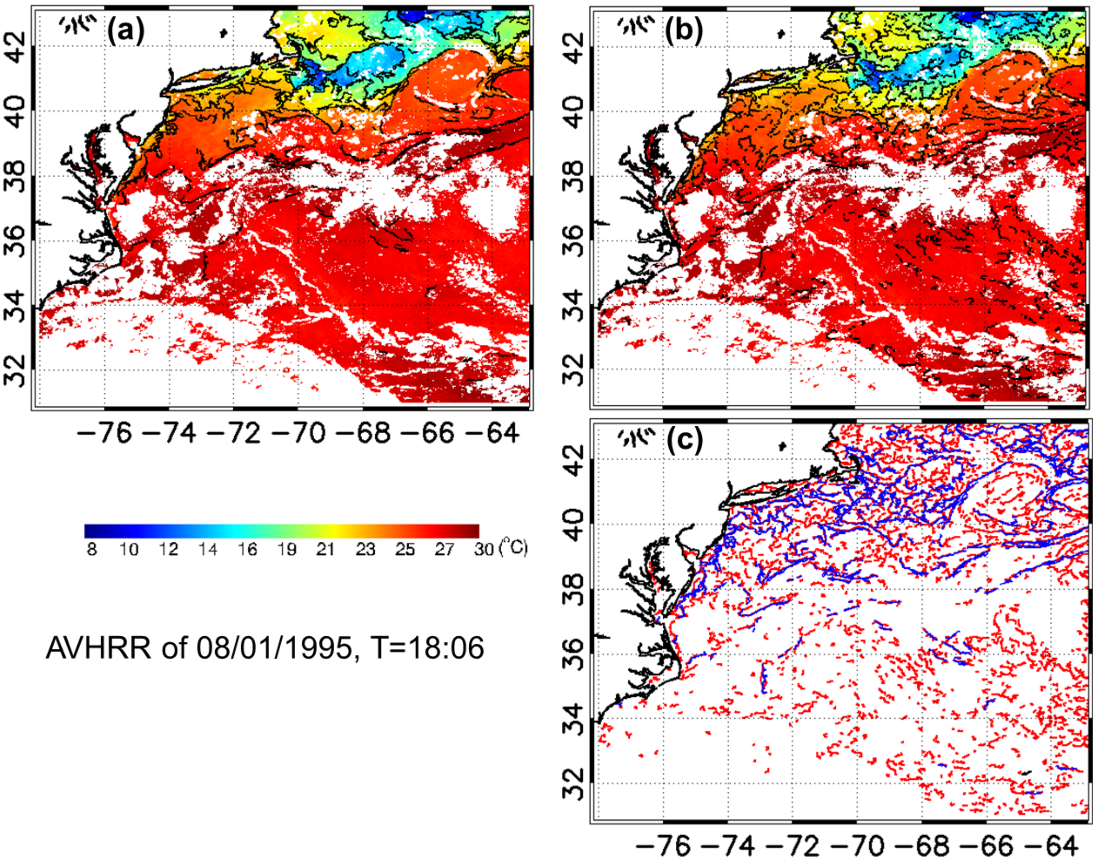
(a)
(b)
(c)
42
40
38
36
34
32
−76 −74 −72 −70 −68 −66 −64
8 10 12 14 16 19 21 23 25 27 30 (°C)
AVHRR of 08/01/1995, T=18:06

Figure 7.

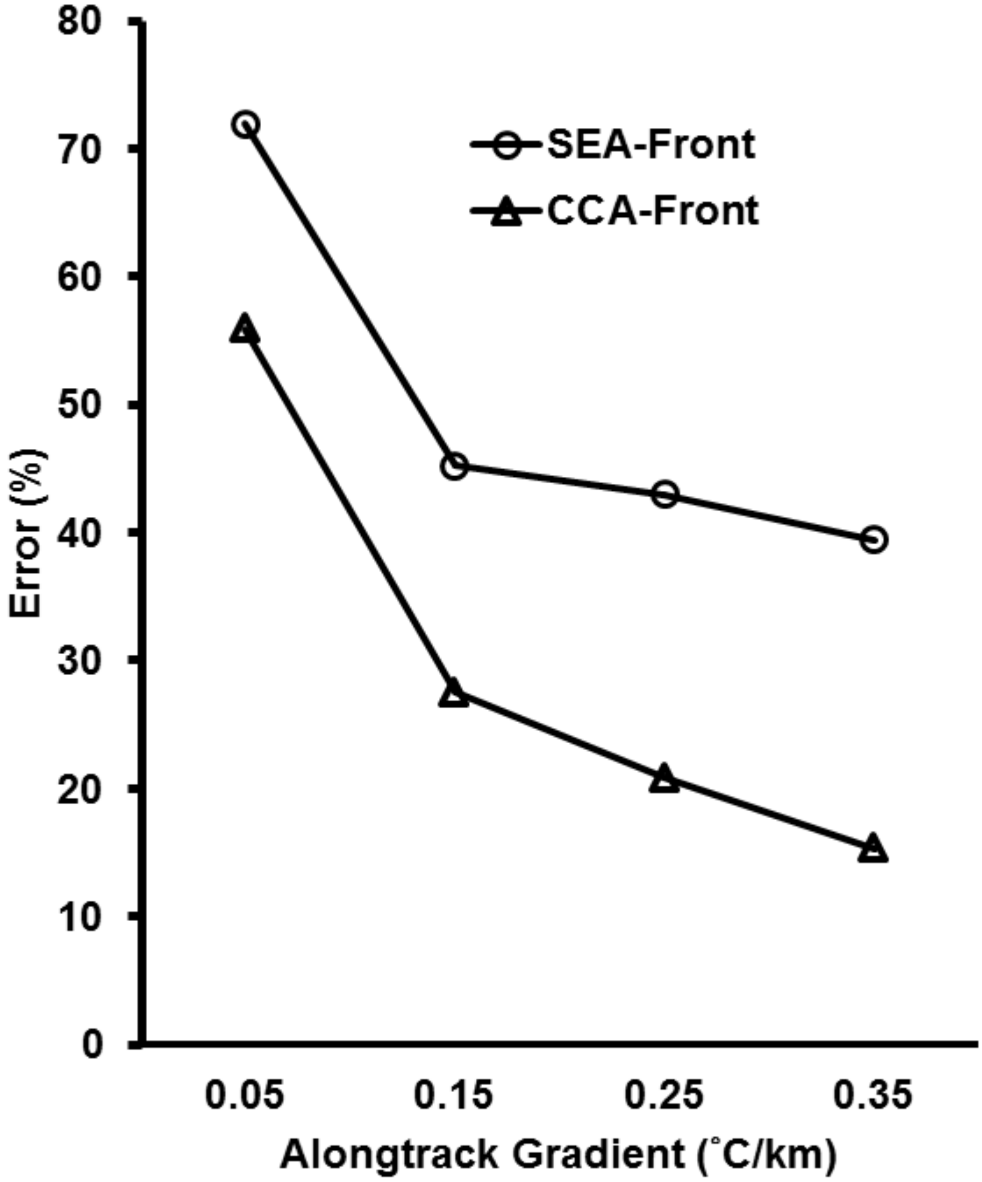
80
70
60
50
40
30
20
10
0
Error (%)
SEA-Front
CCA-Front
0.05
0.15
0.25
0.35
Alongtrack Gradient (˚C/km)

Figure 8.